Ab initio multiconfigurational calculations of experimentally significant energy levels and transition rates in Lr I (Z = 103)

Joseph S. Andrews ⬤,[1,2,3] Andrey I. Bondarev ⬤,[3,4] Per Jönsson ⬤,[5] Jon Grumer ⬤,[6] Sebastian Raeder ⬤,[2,3]
Stephan Fritzsche ⬤,[1,3,4] and Jacek Bieroń ⬤[7]

[1]*Theoretisch-Physikalisches Institut, Friedrich-Schiller-Universität Jena, D-07743 Jena, Germany*
[2]*Helmholtz-Institut Mainz, D-55099 Mainz, Germany*
[3]*GSI Helmholtzzentrum für Schwerionenforschung GmbH, D-64291 Darmstadt, Germany*
[4]*Helmholtz-Institut Jena, D-07743 Jena, Germany*
[5]*Department of Materials Science and Applied Mathematics, Malmö University, S-205 06 Malmö, Sweden*
[6]*Theoretical Astrophysics, Department of Physics and Astronomy, Uppsala University, Box 516, S-751 20 Uppsala, Sweden*
[7]*Instytut Fizyki Teoretycznej, Uniwersytet Jagielloński, 30-348 Kraków, Poland*

Large-scale multiconfigurational calculations are conducted on experimentally significant transitions in Lr I and its lanthanide homologue Lu I, exhibiting good agreement with recent theoretical and experimental results. A single reference calculation is performed, allowing for substitutions from the core within a sufficiently large active set to effectively capture the influence of the core on the valence shells, improving upon previous multiconfigurational calculations. An additional calculation utilizing a multireference set is performed to account for static correlation effects which contribute to the wave function. Reported energies for the two selected transitions are $20\,716 \pm 550\,\mathrm{cm}^{-1}$ and $28\,587 \pm 650\,\mathrm{cm}^{-1}$ for $7s^2 8s\,^2S_{1/2} \rightarrow 7s^2 7p\,^2P^o_{1/2}$ and $7s^2 7d\,^2D_{3/2} \rightarrow 7s^2 7p\,^2P^o_{1/2}$, respectively.

I. INTRODUCTION

Much interest in the actinides has been garnered recently relating to the search for the "island of stability" [1]. The nuclides of the heaviest elements are generally stabilized by nuclear shell effects leading to lifetimes that allow for experimental investigation, although the actual extent of the island remains unknown [2]. Thus, the knowledge of the fundamental nuclear properties as well the influence of the nuclear shell effects in these nuclei is important to understand the limits of matter. Atomic theory can assist in this research by predicting suitable atomic levels in the heaviest elements, which are unveiled using laser spectroscopic techniques. Detailed laser spectroscopy results may be combined with theoretical information on magnetic fields of the electronic shells, electric field gradients, or field shift parameters. This allows the determination of nuclear moments or changes in the nuclear size, respectively.

Such experimental and theoretical collaborations have provided fruitful results for nobelium (No, $Z = 102$) [3], fermium (Fm, $Z = 100$) [4], and for the first ionization potentials of the heavy actinides [5]. There has been a recent focus of attention on neutral lawrencium (Lr I, $Z = 103$), which concludes the actinide series of elements with active $5f$ orbitals. While the first ionization potential was measured by

surface ionization, laser spectroscopic results remain pending. In addition, before the more precise hyperfine splittings of Lr I can be measured, the "broad" energy level structure must first be verified [1].

Various challenges arise from studying Lr I, for experimentalists and theorists alike. Relativistic effects, as well as those of QED are known to influence its atomic structure [6–8]. A comparison between experiment and theory could lead to an examination of the accuracy of multiconfigurational Dirac-Hartree-Fock (MCDHF) based methods at predicting atomic properties at high Z.

The challenges of measuring the atomic properties of lawrencium experimentally are exacerbated by the low production cross section of about 400 nb for the isotope ^{255}Lr in the fusion reaction of a ^{48}Ca beam impinging on a ^{209}Bi target [9]. With a primary beam of 0.8 particle μA, typical target thicknesses of 0.3 mg/cm^2, and a separation efficiency of 30%, this leads to production rates of about 0.4 atoms s^{-1}. High Z elements can be produced at the Separator for Heavy Ion reaction Products (SHIP) at GSI Helmholtzzentrum für Schwerionenforschung in Darmstadt [10,11] and are investigated by laser spectroscopy using the RAdiation-Detected Resonance Ionization Spectroscopy (RADRIS) setup [12,13].

RADRIS, as it stands, can detect transitions from the atomic ground state of Lr I ($7s^2 7p\,^2P^o_{1/2}$) with transition energies between $20\,000$ and $30\,000\,\mathrm{cm}^{-1}$, and with transition rates larger than $10^7\mathrm{s}^{-1}$. Experimental attempts have been made to measure transitions in Lr I, with priority given to those with the highest transition rates [14], but still the uncertainty of the theoretical predictions requires a very large region of several hundred cm^{-1} to be scanned.

While the central scientific motivation for measuring Lr I is driven by an interest in its atomic structure and the subsequent extraction of nuclear properties, various other applications can arise from studying the actinides, such as those in nuclear medicine. Targeted alpha therapy is a particularly exciting area of nuclear medicine in which α-emitting radionuclides are attached to targeting vectors, which can be used to treat various diseases [15].

The ground state of Lr I is predicted to have an opposite parity relative to its lanthanide homologue, neutral lutetium (Lu I) [16], which is attributed to strong relativistic effects. The chemistry of Lr I and its similarity to other elements was investigated by Xu and Pyykkö [17]. From the experimental side, Sato *et al.* [18] measured the ionization potential of Lr I, and Kwarsick *et al.* [19] concluded with the second ionization potential. Sato *et al.* [5] experimentally verified that the $5f$ shell is fully filled at No and confirmed that the actinide series ends with Lr.

Previous calculations of Lr I were conducted using a variety of theoretical methods, including the relativistic coupled cluster approach by Eliav *et al.* [20], and Fock-space coupled-cluster (FSCC) by Borschevsky *et al.* [21]. A calculation of Lr I and other elements using the combination of the configuration interaction with the linearized single-double coupled cluster method (CI + all order) was reported by Dzuba *et al.* [22]. Furthermore, Kahl *et al.* [8] applied the relativistic coupled-cluster method with single, double, and perturbative triple excitations [RCCSD(T)] alongside the configuration interaction combined with many-body perturbation theory (CI + MBPT). Moreover, Guo *et al.* [23] documented the electron affinity and ionization potential of Lr I using the relativistic coupled cluster method.

In addition, the multireference configuration interaction model was used to provide energy levels and spectroscopic properties of the Lr$^+$ ion [24,25]. Energy levels for Lr-like Rf$^+$ were reported by Ramanantoanina *et al.* [26]. Previous MCDHF calculations of Lr I were presented by Wijesundera *et al.* [27], Zou and Froese Fischer [28], and Fritzsche *et al.* [7].

In this paper, Lr I transitions of experimental interest are investigated using the MCDHF method implemented in the GRASP2018 package [29], with minor modifications to ensure sufficient energy convergence and to include configurations with principal quantum numbers $n > 15$.

II. THEORY

To obtain the energy levels of a many-electron system, the eigenvalue problem can be utilized:

$$\hat{H}\Psi = E\Psi. \tag{1}$$

Here Ψ is the atomic state function (ASF) and the Hamiltonian $\hat{H}$ represents the many-electron Dirac-Coulomb (DC) Hamiltonian defined as

$$\hat{H}_{DC} = \sum_{i=1}^{N}[c\boldsymbol{\alpha}_i \cdot \boldsymbol{p}_i + c^2(\beta_i - I) + V_{\text{nuc}}(r_i)] + \sum_{j>i=1}^{N}\frac{1}{r_{ij}}, \tag{2}$$

where r_{ij} represents the distance between electrons i and j, N is the total number of electrons in the system, c is the speed of light, α and β are the Dirac matrices, and $V_{\text{nuc}}(r)$ is the nuclear potential arising from the two-parameter Fermi distribution function [30]; atomic units ($\hbar = e = m_e = 1$) are used throughout.

In the standard formulation of the MCDHF theory, the function Ψ for a given state is represented as a linear combination of symmetry-adapted configuration state functions (CSFs)

$$\Psi(\Gamma\pi JM) = \sum_{i=1}^{N_{\text{CSF}}} c_i\Phi(\gamma_i\pi JM). \tag{3}$$

Here J is the total electronic angular momentum, M is its projection, π is the parity, γ_i denotes the set of orbital occupancies and complete coupling tree of angular quantum numbers unambiguously specifying the ith CSF, and Γ is the identifying label, which contains all the other necessary information to uniquely describe the state function. Configuration mixing coefficients c_i are obtained through diagonalization of the Hamiltonian matrix.

The relativistic configuration interaction (RCI) method is used to calculate configuration mixing coefficients c_i without altering the orbital shapes. Corrections to the DC Hamiltonian such as the transverse photon interaction (which simplifies to the Breit interaction in the low-frequency limit), and leading-order QED corrections are included using RCI.

After obtaining a set of atomic state functions, the transition rates for an electric dipole transition between two atomic states Ψ_i and Ψ_f can be calculated using the reduced transition matrix element [31] of the electric dipole transition operator $\mathbf{D}^{(1)}$:

$$M_{if} = \langle\Psi_i||\mathbf{D}^{(1)}||\Psi_f\rangle. \tag{4}$$

Explicit expressions for the operator can be found in Refs. [32–34]. In the Coulomb gauge, which is used in the present calculations, the matrix element of the operator in the low-frequency limit can be written as

$$\frac{1}{E_f - E_i}\sum_{j=1}^{N}\langle\Psi_i||\nabla^{(1)}(j)||\Psi_f\rangle. \tag{5}$$

The latter expression is also referred to as the velocity form.

III. MODELS

Dirac-Hartree-Fock (DHF) wave functions of Lr I involve only a single CSF for each total angular momentum J and parity π, representing the simplest approximation of the atomic system. However, DHF calculations are limited because they do not fully account for electron-electron repulsion, as a result of its mean-field approximation. To better account for the repulsion between electrons, additional CSFs are systematically included into the wave function expansion. The electron correlation energy is the energy due to unaccounted electron-electron repulsion and is defined as the difference between DHF calculations and verified experimental results from the NIST ASD [35], which are assumed to be exact for the purposes of this study. The CSFs accounting for the repulsion of the electrons are built from an active set (AS) of orbitals. The AS is systematically increased to include additional

correlation orbitals as layers $\mathcal{L}_i$; a layer is defined as a set of orbitals that includes at maximum one of each orbital angular momentum symmetry, $\ell \leqslant 4$ or $\ell = \{s, p, d, f, g\}$. An additional layer increases the AS such that the AS becomes a union of the DHF spectroscopic orbitals and the layers, represented as AS : DHF $\cup$ $\mathcal{L}_1 \cup \mathcal{L}_2 \cup \mathcal{L}_3$ for an AS involving three layers.

The targeted states in Lr I are the ground state $7s^2 7p\ ^2P^o_{1/2}$ and the excited levels $7s^2 8s\ ^2S_{1/2}$, $7s^2 6d\ ^2D_{3/2,5/2}$ and $7s^2 7d\ ^2D_{3/2,5/2}$. The $7s^2 7p\ ^2P^o_{3/2}$ level is also included to ensure that both the $7p_{1/2}$ and $7p_{3/2}$ orbitals are optimized. The results of previous calculations suggest that energies and rates of transitions from these excited states to the ground state are within the requirements of RADRIS [8,13]. To ensure computational feasibility, the number of CSFs was chosen to balance the accuracy of the wave function with the limitations of the computational hardware.

In quantum chemistry, electron correlation is typically divided into two categories, static correlation and dynamic correlation. Static correlation arises in atomic systems when levels are nearly degenerate in the DHF energies, whereas dynamic correlation arises from the dynamic motions of electrons within a correlated system [36]. Static correlation is resolved in MCDHF by employing a multireference (MR) set [37], while dynamic correlation is more challenging and is resolved by systematically adding CSFs built from increasing the active sets of orbitals. We perform a set of single reference (SR) calculations to include core correlation contributions to the wave function. A separate set of calculations are performed to account for unincluded static correlation. By including both types of these calculations, all major types of electron correlation are accounted for.

Several factors indicate that the interelectronic interaction involving the $5d$ and $5f$ core subshells contributes to the energy separations. In a heavy and neutral system, the screening effect of the inner shells diminishes the nuclear charge's influence more strongly, enhancing the core electrons influence upon the energy separations. Additionally, the unpaired electron in Lr I strongly polarizes the core.

The calculation is divided up into four major stages or models. With each sequential model, additional correlation effects are included and the calculation is expected to become more accurate. For the SR set, the calculations proceed as follows: Model One → Model Two → Model Three → Model Four. For the MR set, the logical flow is: MR Model One → MR Model Two → MR Model Three. Although similar procedures apply to the SR and MR models, the MR and SR set calculations are performed independently and do not infer from each other.

Model One. This stage of the calculations involves optimizing the spectroscopic orbitals. The spectroscopic orbitals are optimized using DHF, whereby no electron substitutions are allowed from the reference set to ensure each orbital has the correct number of nodes, or number of regions where the wave function changes sign. The targeted even parity levels are $7s^2 8s\ ^2S_{1/2}$, $7s^2 6d\ ^2D_{3/2,5/2}$, $7s^2 7d\ ^2D_{3/2,5/2}$ and the targeted odd parity levels are $7s^2 7p\ ^2P^o_{1/2,3/2}$. The $7s^2 6d\ ^2D_{3/2,5/2}$ levels are not included in Model Four due to computational limitations.

In Lu I, analogous levels are targeted. The targeted even parity levels are $6s^2 7s\ ^2S_{1/2}$, $6s^2 5d\ ^2D_{3/2,5/2}$ and the odd parity levels are $6s^2 6p\ ^2P^o_{1/2,3/2}$. As the $6s^2 6d\ ^2D_{3/2,5/2}$ levels are relatively high-lying in energy, these could not be optimized correctly, and were not included in the calculation.

Model Two. The next stage of the calculations involves generating and optimizing the correlation orbitals. The strategy suggested by Papoulia *et al.* [38] was employed. The MCDHF method as implemented in GRASP2018 is unable to optimize all correlation orbitals simultaneously, requiring the user to adopt the layer-by-layer optimization strategy [39]. Correlation orbitals are generated by allowing single and double (SD) substitutions from the valence shells $6d$, $7s$, $7p$, $7d$, and $8s$ ($5d$, $6s$, $6p$, and $7s$) in Lr I (Lu I). SD substitutions are chosen to account for dynamic correlation by accurately modeling electron-electron repulsions between two electrons.

The electric dipole transitions between the targeted states in Lr I only involve valence electron jumps. While optimizing the correlation orbitals, core substitutions were not allowed to ensure the correlation orbitals better model electron correlation in the valence orbitals and are in a close radial proximity to the valence as a result. The AS is systematically increased up to layer ten in Lr I with orbitals $\mathcal{L}_{10} = \{17s, 16p, 16d, 14f, 13g\}$.

Model Three. The third stage of the calculation utilizes the relativistic configuration interaction program RCI as implemented in GRASP2018 [29]. SD electron substitutions from the previously defined valence orbitals and the $\{6s, 6p\}$ ($\{5s, 5p\}$) subshells in Lr I (Lu I) were allowed to expand the CSF basis set and account for core correlation effects. Also at this stage included in the Hamiltonian were further relativistic effects: the transverse photon interaction (often referred to as the Breit interaction, see Sec. 3.7 of Ref. [40]), as well as the leading QED corrections, vacuum polarization and self-energy (see Secs. 2.3 and 2.8 of Ref. [41]). Initial calculations suggest these effects have only a minor impact on the energy separations, resulting in an average decrease in energy of the targeted excited states relative to the ground state of $35\ \mathrm{cm}^{-1}$.

Figure 1 shows the average radius of the spectroscopic subshells in Lr I. The correlation orbitals are optimized to be in close proximity to the valence orbitals. Furthermore, the $\{6s, 6p\}$ subshells are close to the valence, suggesting these would have the greatest effect on the energy separations.

Model Four. In the fourth and largest model, RCI is run to improve the wave-function representation by employing a larger basis set. Further relativistic effects such as Breit, as well as QED effects are included as a correction to the wave function at this stage. SD electron substitutions are allowed in Lr I (Lu I) from the $\{6s, 6p\}$ ($\{5s, 5p\}$) subshells. In addition, single and restricted double (SrD) substitutions are allowed from the $\{5d, 5f\}$ ($\{4d, 4f\}$) subshells [42]. The SrD substitutions are a restriction to SD where in total two electrons are substituted, however, at maximum only one electron may be substituted from any of the $\{5d, 5f\}$ ($\{4d, 4f\}$) subshells. The $7s^2 6d\ ^2D_{3/2,5/2}$ levels could not be included in Model Four due to computational limitations. The SrD method is designed to model core-valence correlation effects without considering costly core-core correlation effects, which are expected to have a negligible impact on energy separations.
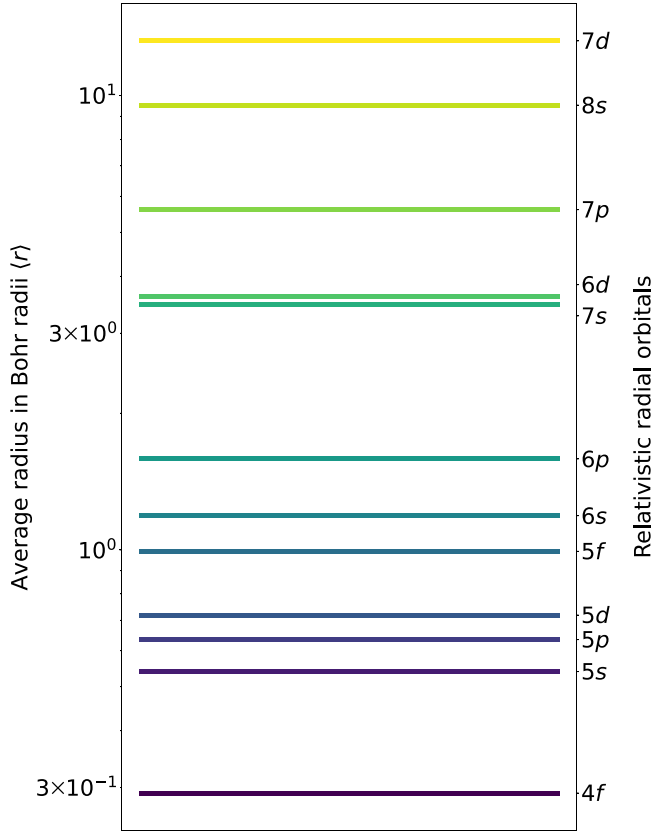
FIG. 1. The average radii in Bohr radii of the spectroscopic relativistic radial orbitals in Lr I. Only radial orbitals with total angular momentum $j = l + 1/2$ are included for clarity. The subshells are colored based upon their average distance from the nucleus.

To address the effects of static correlation, a multireference (MR) set is created which includes configurations with the largest contribution to the wave function. To obtain the configurations with the greatest contribution, a small test calculation was conducted in SR with two layers using Model Two. Configurations from this calculation were sorted by mixing coefficient and added to the MR set until the cumulative mixing coefficients reached 95% of the wavefunction. Calculations were performed with the MR set similarly to the main SR calculation for consistency, with the exception that the MR calculation does not use Model Four due to computational limitations.

MR Model One. For the first stage of the MR calculation, the Lr I MR set includes the odd parity configuration $7s6d7p$ in addition to the $7s^2 7p$ configuration and the even parity configuration $7s7p^2$ in addition to the $7s^2 8s$, $7s^2 6d$ and $7s^2 7d$ configurations. The spectroscopic orbitals were optimized using DHF. The targeted even parity levels were $7s^2 8s\ ^2S_{1/2}$, $7s^2 6d\ ^2D_{3/2,5/2}$, $7s^2 7d\ ^2D_{3/2,5/2}$ and the targeted odd parity levels are $7s^2 7p\ ^2P^o_{1/2,3/2}$.

The calculation is repeated for lutetium, the Lu I MR set includes the odd parity configuration $6s5d6p$ in addition to the $6s^2 6p$ configuration, and the even parity configurations $6s5d^2$, $6s6p^2$ are included in addition to the $6s^2 7s$, $6s^2 5d$ configurations. For Lu I, analogous levels were targeted. The

even parity targeted levels are $6s^2 7s\ ^2S_{1/2}$, $6s^2 5d\ ^2D_{3/2,5/2}$ and the odd parity levels are $6s^2 6p\ ^2P^o_{1/2,3/2}$.

MR Model Two. In the second stage of the MR calculation, correlation orbitals are generated and optimized. Correlation orbitals are generated by allowing single and double (SD) substitutions from the valence shells $6d$, $7s$, $7p$, $7d$ and $8s$ ($5d$, $6s$, $6p$ and $7s$) from the Lr I (Lu I) MR set.

MR Model Three. In the third and final stage of the MR calculation, SD substitutions from the previously defined valence shells and electron substitutions from the $\{6s, 6p\}$ ($\{5s, 5p\}$) subshells were allowed to further expand the CSF basis and consider core contributions. A calculation is performed on the expanded CSF basis set using RCI, further relativistic and QED effects are included as a correction to the wave function.

IV. RESULTS AND DISCUSSION

Figures 2(a)–2(f) show how the calculations converge as the AS is systematically increased. The total energy of the system decreases as the AS increases, however, the even and odd parities will decrease at a different rate, agreeing at convergence [43]. Allowing substitutions from the core magnifies oscillations due to the large amounts of correlation associated with the core, and increasing the size of the AS is required to compensate this. Model Four is designed to capture all leading dynamic correlation contributions, while the MR Model Three calculations are designed to capture static correlation effects. Unfortunately, it is not currently computationally feasible to perform calculations of Lr I that fully account for both static and dynamic correlation. To account for both types of electron correlation, a method is proposed to calculate the change in energy separations as a result of accounting for static electron correlation.

Table I presents the results of the SR and MR calculations of Lu I and Lr I. These indicate that using Model Four is essential for achieving good agreement between the even and odd parity energy levels. However, Model Four is computationally infeasible with the MR.

As a result, the contributions due to the MR are computed by considering only the change in energy between SR Model Three and MR Model Three for that level and the ground-state level of the same parity.

Our method calculates the total energy by taking the value of the energy for a level in Model Four and adding the energy difference due to the inclusion of the MR set, which is derived from the energy differences of levels with the same parity

$$E_{\text{Total}} = E_{\text{Dynamic}} + E_{\text{Static}}$$
$$= E_{\text{Model Four}} + \Delta E_{\text{MR}}. \quad (6)$$

For the case of the $7s^2 8s\ ^2S_{1/2}$ energy level in Lr I (Table I), the change in energy due to the inclusion of the MR set, ΔE_{MR}, is computed as $(22\,003 - 4853) - (19\,930 - 3145) = 365\,\text{cm}^{-1}$, which can be then combined with the Model Four result to give the total energy separation.

For all excited levels in Lr I, ΔE_{MR} is positive, meaning that including the MR leads to an increase in parity-relative energy separations. Similarly, the effect of accounting for additional core correlation appears to be an increase in parity-relative energy separations.
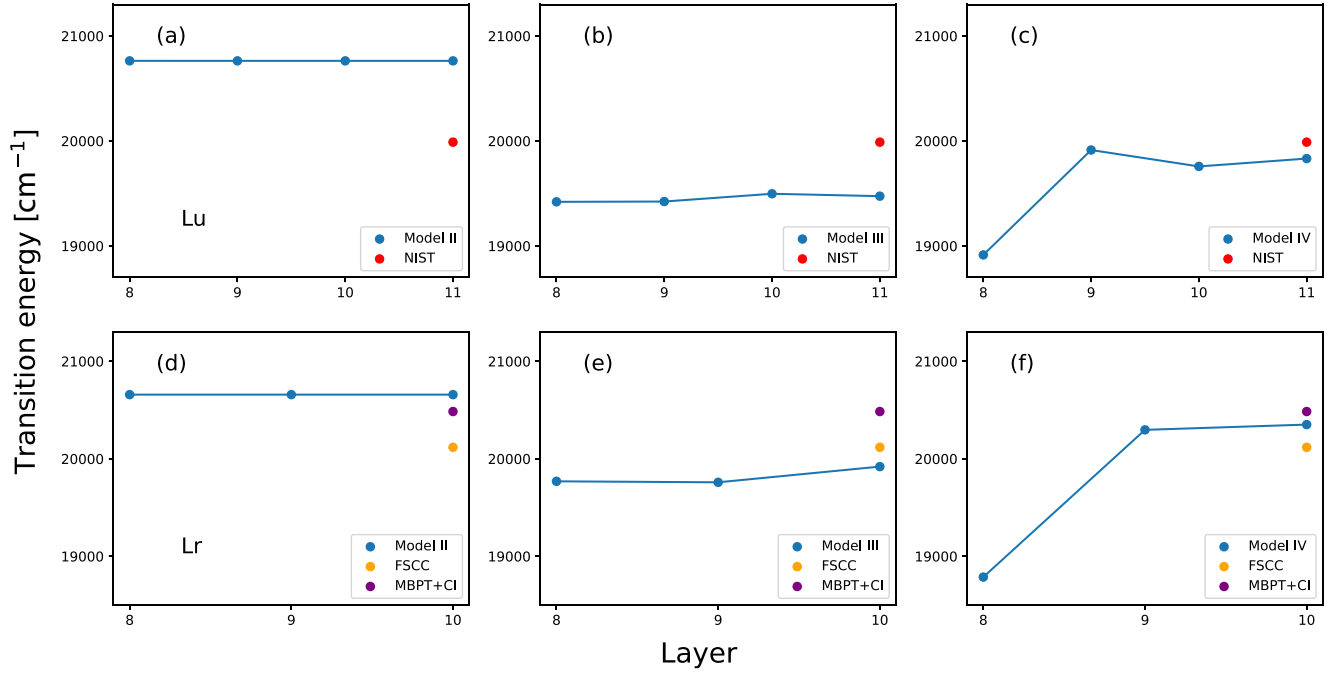
FIG. 2. MCDHF calculations of the transition energy for the last four computational layers of Lr I (Lu I), as a function of computational layer for the transition of $7s^2 8s\,{}^2S_{1/2} \rightarrow 7s^2 7p\,{}^2P^o_{1/2}$ ($6s^2 7s\,{}^2S_{1/2} \rightarrow 6s^2 6p\,{}^2P^o_{1/2}$). The upper three subfigures (a)–(c) present the results for Lu I while the lower three subfigures (d)–(f) present the results for Lr I. The subfigures from left to right show how the calculations evolve as the computational model becomes larger and more core correlation is considered. The subfigures on the left (a), (d) show the transition energies for Model Two, when only valence effects are considered. The middle subfigures (b), (e) show the transition energies for Model Three. The subfigures to the right (c), (f) show the transition energies for Model Four. The calculations of Lr I are compared to the results of the previous theoretical calculations using FSCC [21] and CI + MBPT [8], while the calculations of Lu I are compared to experimental values from NIST [35].

Notably, after applying this method the $6s^2 7s\,{}^2S_{1/2}$ level in the Total column in Table I is remarkably close to the NIST value. However, the $6s^2 5d\,{}^2D_{5/2}$ level becomes further from the NIST value. Possible explanations for this could include an unbalanced MR between the ground and excited energy levels. The $7s^2 6d\,{}^2D_{3/2,5/2}$ levels could not be included in Model

Four due to computational limitations. Table II shows the calculated transition rates in the Coulomb gauge for Lu I and Lr I across the different models, and compares these to both experiment and previous theory. Interestingly, the Lu I calculations are close to the experimental values for Model Two and the MR Model Three, but not accurate for Models

TABLE I. The calculated energy levels of Lr I and Lu I for different computational models, details on the different models are discussed in Sec. III. The results are compared to NIST [35] where available, the values in the "Total" column are obtained by considering the effects of both static and dynamic correlation.

Levels			Energy (cm^{-1})						
Element	Configuration	Term	Model Two	Model Three	MR Model Three	ΔE_{MR}	Model Four	Total	NIST
Lu	$6s^2 5d$	${}^2D_{3/2}$	0	0	0	0	0	0	0
	$6s^2 5d$	${}^2D_{5/2}$	1334	1695	1619	−76	1778	1702	1993
	$6s^2 6p$	${}^2P^o_{1/2}$	590	3548	2358	0	3864	3864	4136
	$6s^2 6p$	${}^2P^o_{3/2}$	3765	6866	5686	10	7220	7230	7476
	$6s^2 7s$	${}^2S_{1/2}$	21353	23023	23523	500	23717	24217	24125
Lr	$7s^2 7p$	${}^2P^o_{1/2}$	0	0	0	0	0	0	—
	$7s^2 6d$	${}^2D_{3/2}$	4907	3145	4853	0	—	—	—
	$7s^2 6d$	${}^2D_{5/2}$	7106	6047	7763	8	—	—	—
	$7s^2 7p$	${}^2P^o_{3/2}$	8133	8283	8540	257	8223	8480	—
	$7s^2 8s$	${}^2S_{1/2}$	20658	19930	22003	365	20351	20716	—
	$7s^2 7d$	${}^2D_{3/2}$	28543	27700	29922	514	28073	28587	—
	$7s^2 7d$	${}^2D_{5/2}$	28694	27949	30166	509	28277	28786	—

TABLE II. The calculated transition rates in the Coulomb gauge for Lu I and Lr I are showcased for different computational models, the results of Lu I are compared to NIST [35] and Lr I is compared to CI + MBPT [8]. The Lu I transition rates of Models Two and Three had poor energy separations and were scaled with the factor $\lambda_{\text{Calculated}}^3/\lambda_{\text{NIST}}^3$ where λ is the transition wavelength to allow comparison between models.

| | Upper levels | | Lower levels | | Einstein A coefficient (s^{-1}) | | | | |
Element	Conf.	Term	Conf.	Term	Model Two	Model Three	Model Four	MR Model Three	NIST/CI+MBPT
Lu	$6s^27s$	$^2S_{1/2}$	$6s^26p$	$^2P_{1/2}^o$	3.14×10^7	4.10×10^7	4.21×10^7	3.21×10^7	3.20×10^7
	$6s^27s$	$^2S_{1/2}$	$6s^26p$	$^2P_{3/2}^o$	5.23×10^7	6.94×10^7	7.25×10^7	5.45×10^7	4.9×10^7
Lr	$7s^28s$	$^2S_{1/2}$	$7s^27p$	$^2P_{1/2}^o$	3.13×10^7	3.41×10^7	3.30×10^7	3.38×10^7	3.31×10^7
	$7s^27d$	$^2D_{3/2}$	$7s^27p$	$^2P_{1/2}^o$	5.03×10^7	4.91×10^7	4.61×10^7	3.95×10^7	6.14×10^7
	$7s^28s$	$^2S_{1/2}$	$7s^27p$	$^2P_{3/2}^o$	3.31×10^7	3.34×10^7	3.39×10^7	2.88×10^7	3.57×10^7
	$7s^27d$	$^2D_{3/2}$	$7s^27p$	$^2P_{3/2}^o$	9.57×10^6	9.80×10^6	9.75×10^6	6.94×10^6	1.21×10^7
	$7s^27d$	$^2D_{5/2}$	$7s^27p$	$^2P_{3/2}^o$	3.68×10^7	5.19×10^7	5.19×10^7	3.92×10^7	5.39×10^7

Three and Four, this shows the importance of including the MR when calculating transition rates.

Model Two can mimic the MR calculation by allowing SD substitutions between the valence shells, allowing many different configurations to be created. However, the same is not true for Models Three and Four.

In Models Three and Four, where core substitutions are allowed, if one electron moves from a valence shell to another to make a new valence configuration, only one core electron can be substituted due to the SD restriction. This single core substitution is inadequate for accurately representing electron-electron interactions in the core, resulting in the new configuration having a relatively minimal contribution to the system's total energy. This may be resolved by either allowing single, double and triple (SDT) electron substitutions or by conducting a calculation with an MR set.

Given the difference in transition rates between Models Three and Four are small, it is assumed that the difference between MR Model Three and a hypothetical MR Model Four would also be negligible. Therefore, results from experiment and previous theory are compared to MR Model Three. As Models Two and Three in Lr I yield energy separations that deviate significantly from the NIST values, these transition rates are adjusted by the factor $\lambda_{\text{Calculated}}^3/\lambda_{\text{NIST}}^3$ to align with the experimental energy separations and to allow comparison between models.

The Lu I and Lr I transition rates are compared to NIST and CI + MBPT [8], respectively. The Lu I transition rates show excellent agreement with experiment with the differences between NIST being 0.3 and 11% for the two calculated transitions in Table II. The calculated transition rates of Lr I also show good agreement with previous theory, especially

for transitions originating from the upper level of $7s^28s\,^2S_{1/2}$, which show deviations of 2.1% and 23% compared to CI + MBPT. Although the transition rates from the $7s^27d\,^2D_{3/2,5/2}$ upper levels are approximately 35% larger than the values in MR Model Three, this discrepancy is within the uncertainity of 40% estimated by Kahl *et al.* [8].

Table III presents a comparison between our calculated results and previous theoretical values, with our results showing the closest agreement with the recent CI + MBPT and RCCSD(T) values reported by Kahl *et al.* [8]. Previous MCDHF calculations reported the $7s^27p\,^2P_{3/2}^o - 7s^27p\,^2P_{1/2}^o$ energy to be lower than our value. This may be attributed to the limited inclusion of electron correlation in those studies.

Our calculations improve upon those of Zou and Froese Fischer [28] and Fritzsche *et al.* [7] which did not include the effects of the *g* correlation orbitals and core contributions from the 5*d* orbitals, respectively. The *g* correlation orbitals are important for describing the actinides since these orbitals have a direct dipole interaction with the 5*f* core orbitals [7]. Furthermore, due to the computational constraints that existed at the time, convergence is not demonstrated in either work as only two layers were included in the calculations.

Uncertainty

Assuming the uncertainties are independent and uncorrelated, the total energy uncertainty can be calculated as the square root of the sum of the squares of the dynamic and static energy uncertainties [44].

The uncertainty in energy is calculated for the transitions from the upper levels $7s^28s\,^2S_{1/2}$, $7s^27d\,^2D_{3/2}$ to the ground state $7s^27p\,^2P_{1/2}^o$. The static uncertainty is taken to be the differ-

TABLE III. The calculated energy levels of experimental significance of Lr I in comparison to previous theory.

| Levels | | Energy (cm^{-1}) | | | | | | |
Configuration	Term	This work	CI + MBPT [8]	RCCSD(T) [8]	FSCC [21]	CI + all order [22]	MCDHF [7]	MCDHF [28]
$7s^27p$	$^2P_{1/2}^o$	0	0	0	0	0	0	0
$7s^27p$	$^2P_{3/2}^o$	8480	8606	8677	8413	8495	8138	7807
$7s^28s$	$^2S_{1/2}$	20736	20485	20533	20118	20253	20405	—
$7s^27d$	$^2D_{3/2}$	28607	28580	—	28118	—	—	—
$7s^27d$	$^2D_{5/2}$	28806	28725	—	28385	—	—	—

ence between the MR Model Three energy relative to the lowest energy level of the same parity and the Model Three energy relative the lowest energy level of the same parity in Table I. This is calculated to be $365\,\mathrm{cm}^{-1}$ and $514\,\mathrm{cm}^{-1}$ for the $7s^2 8s\,^2S_{1/2}$ and $7s^2 7d\,^2D_{3/2}$ levels, respectively.

The dynamic uncertainty is taken to be the difference between the NIST ASD and the Lu I Model Four values. The corresponding level of the $7s^2 8s\,^2S_{1/2}$ level in lutetium is the $6s^2 7s\,^2S_{1/2}$ level, the dynamic uncertainty for this level is determined to be $408\,\mathrm{cm}^{-1}$. The $7s^2 7d\,^2D_{3/2}$ level has no lutetium equivalent due to computational limitations, therefore it is assumed the dynamic uncertainty for this level is the same as for level $7s^2 8s\,^2S_{1/2}$.

The total uncertainty can be obtained by taking the square root of the sum of the squares of the two uncertainties, this is then rounded to the nearest $50\,\mathrm{cm}^{-1}$. The uncertainty of the $7s^2 8s\,^2S_{1/2}$ level in Lr I is reported as $547\,\mathrm{cm}^{-1}$, rounded to $550\,\mathrm{cm}^{-1}$ while the uncertainty of the $7s^2 7d\,^2D_{3/2}$ level is $656\,\mathrm{cm}^{-1}$, rounded to $650\,\mathrm{cm}^{-1}$.

V. CONCLUSION

We report calculated values of experimentally significant energy levels and corresponding transition rates of Lr I and its lighter homologue Lu I, obtained using the MCDHF method as implemented in GRASP2018. Calculations were performed with various computational models with and without a multireference set to capture different types of electron correlation.

The reported transitions energies are $20\,716 \pm 550\,\mathrm{cm}^{-1}$ for the atomic transition $7s^2 8s\,^2S_{1/2} \rightarrow 7s^2 7p\,^2P^o_{1/2}$ and $28\,587 \pm 650\,\mathrm{cm}^{-1}$ for the $7s^2 7d\,^2D_{3/2} \rightarrow 7s^2 7p\,^2P^o_{1/2}$ atomic transition. This work improves upon previous MCDHF calculations by Zou and Froese Fischer [28] and Fritzsche *et al.* [7] by demonstrating convergence and by considering the effects of the *g* correlation orbitals and core contributions

from the 5*d* orbitals. Calculated energy levels and transition rates of Lu I and Lr I exhibited good agreement with experiment and previous theory, respectively. Our work on Lr I appears to be in closest agreement with the theoretical calculations performed using CI + MBPT and RCCSD(T) [8]. The demonstrated agreement within different atomic theory frameworks will help the effort of experimental level search in Lr I as it clearly restrains the region which needs to be investigated. The uncertainties of the calculated energy levels, arising from limited computational resources, were quantified and remain large compared to the discrepancies observed in individual recent theoretical calculations.

Future calculations may include a multireference model variationally to consider both static and dynamic correlation within a large active set. To accomplish this, new methods could be utilized such as independently optimized orbital sets [45] or machine learning [46] to reduce the computational load.

DATA AVAILABILITY

The data that support the findings of this article are openly available [47].

[1] M. Block, M. Laatiaoui, and S. Raeder, Prog. Part. Nucl. Phys. **116**, 103834 (2021).

[2] O. Smits, P. Indelicato, W. Nazarewicz, M. Piibeleht, and P. Schwerdtfeger, Phys. Rep. **1035**, 1 (2023).

[3] M. Laatiaoui, W. Lauth, H. Backe, M. Block, D. Ackermann, B. Cheal, P. Chhetri, C. E. Düllmann, P. Van Duppen, J. Even *et al.*, Nature (London) **538**, 495 (2016).

[4] J. Warbinek, E. Rickert, S. Raeder, T. Albrecht-Schönzart, B. Andelic, J. Auler, B. Bally, M. Bender, S. Berndt, M. Block *et al.*, Nature (London) **634**, 1075 (2024).

[5] T. K. Sato, M. Asai, A. Borschevsky, R. Beerwerth, Y. Kaneya, H. Makii, A. Mitsukai, Y. Nagame, A. Osa, A. Toyoshima *et al.*, J. Am. Chem. Soc. **140**, 14609 (2018).

[6] K. Kozioł and G. A. Aucar, J. Chem. Phys. **148**, 134101 (2018).

[7] S. Fritzsche, C. Z. Dong, F. Koike, and A. Uvarov, Euro. Phys. J. D **45**, 107 (2007).

[8] E. V. Kahl, S. Raeder, E. Eliav, A. Borschevsky, and J. C. Berengut, Phys. Rev. A **104**, 052810 (2021).

[9] H. Gäggeler, D. Jost, A. Türler, P. Armbruster, W. Brüchle, H. Folger, F. Heßberger, S. Hofmann, G. Münzenberg, V. Ninov *et al.*, Nucl. Phys. A **502**, 561 (1989).

[10] G. Münzenberg, W. Faust, S. Hofmann, P. Armbruster, K. Güttner, and H. Ewald, Nucl. Instrum. Methods **161**, 65 (1979).

[11] M. Block, F. Giacoppo, F.-P. Heßberger, and S. Raeder, Riv. Nuovo Cim. **45**, 279 (2022).

[12] F. Lautenschläger, P. Chhetri, D. Ackermann, H. Backe, M. Block, B. Cheal, A. Clark, C. Droese, R. Ferrer, F. Giacoppo *et al.*, Nucl. Instrum. Methods Phys. Res., Sect. B **383**, 115 (2016).

[13] J. Warbinek, B. Anđelić, M. Block, P. Chhetri, A. Claessens, R. Ferrer, F. Giacoppo, O. Kaleja, T. Kieck, E. Kim *et al.*, Atoms **10**, 41 (2022).

[14] J. Warbinek (private communication).

[15] B. J. B. Nelson, J. D. Andersson, and F. Wuest, Pharmaceutics **13**, 49 (2020).

[16] J.-P. Desclaux and B. Fricke, Journal de Physique **41**, 943 (1980).

[17] W.-H. Xu and P. Pyykkö, Phys. Chem. Chem. Phys. **18**, 17351 (2016).

[18] T. K. Sato, M. Asai, A. Borschevsky, T. Stora, N. Sato, Y. Kaneya, K. Tsukada, Ch. E. Düllmann, K. Eberhardt, E. Eliav *et al.*, Nature (London) **520**, 209 (2015).

[19] J. T. Kwarsick, J. L. Pore, J. M. Gates, K. E. Gregorich, J. K. Gibson, J. Jian, G. K. Pang, and D. K. Shuh, J. Phys. Chem. A **125**, 6818 (2021).

[20] E. Eliav, U. Kaldor, and Y. Ishikawa, Phys. Rev. A **52**, 291 (1995).

[21] A. Borschevsky, E. Eliav, M. J. Vilkas, Y. Ishikawa, and U. Kaldor, Euro. Phys. J. D **45**, 115 (2007).

[22] V. A. Dzuba, M. S. Safronova, and U. I. Safronova, Phys. Rev. A **90**, 012504 (2014).

[23] Y. Guo, L. F. Pašteka, Y. Nagame, T. K. Sato, E. Eliav, M. L. Reitsma, and A. Borschevsky, Phys. Rev. A **110**, 022817 (2024).

[24] H. Ramanantoanina, A. Borschevsky, M. Block, and M. Laatiaoui, Atoms **10**, 48 (2022).

[25] H. Ramanantoanina, A. Borschevsky, M. Block, L. Viehland, and M. Laatiaoui, Phys. Rev. A **108**, 012802 (2023).

[26] H. Ramanantoanina, A. Borschevsky, M. Block, and M. Laatiaoui, Phys. Rev. A **104**, 022813 (2021).

[27] W. P. Wijesundera, S. H. Vosko, and F. A. Parpia, Phys. Rev. A **51**, 278 (1995).

[28] Y. Zou and C. Froese Fischer, Phys. Rev. Lett. **88**, 183001 (2002).

[29] C. Froese Fischer, G. Gaigalas, P. Jönsson, and J. Bieroń, Comput. Phys. Commun. **237**, 184 (2019).

[30] F. A. Parpia and A. K. Mohanty, Phys. Rev. A **46**, 3735 (1992).

[31] B. Atalay, T. Brage, P. Jönsson, and H. Hartman, Astronomy & Astrophysics **631**, A29 (2019).

[32] I. P. Grant, J. Phys. B **7**, 1458 (1974).

[33] Edited by I. P. Grant, *Relativistic Quantum Theory of Atoms and Molecules*, Springer Series on Atomic, Optical, and Plasma Physics, Vol. 40 (Springer, New York, 2007).

[34] W. R. Johnson, *Atomic Structure Theory: Lectures on Atomic Physics* (Springer, Berlin, 2007).

[35] A. Kramida, Yu. Ralchenko, J. Reader, and NIST ASD Team, NIST Atomic Spectra Database (ver. 5.11) (National Institute of Standards and Technology, Gaithersburg, MD, 2023), https://physics.nist.gov/asd.

[36] C. Froese Fischer, T. Brage, and P. Jönsson, *Computational Atomic Structure: An MCHF Approach* (Institute of Physics, Bristol, England, 1997).

[37] R. R. Li and M. R. Hoffmann, *Advances in Quantum Chemistry* (Elsevier, Amsterdam, 2020), Vol. 81, pp. 105–141.

[38] A. Papoulia, J. Ekman, G. Gaigalas, M. Godefroid, S. Gustafsson, H. Hartman, W. Li, L. Radžiūtė, P. Rynkun, S. Schiffmann *et al.*, Atoms **7**, 106 (2019).

[39] S. Schiffmann, M. Godefroid, J. Ekman, P. Jönsson, and C. Froese Fischer, Phys. Rev. A **101**, 062510 (2020).

[40] P. Jönsson, G. Gaigalas, C. Froese Fischer, J. Bieroń, I. P. Grant, T. Brage, J. Ekman, M. Godefroid, J. Grumer, J. Li, and W. Li, Atoms **11**, 68 (2023).

[41] P. Jönsson, M. Godefroid, G. Gaigalas, J. Ekman, J. Grumer, W. Li, J. Li, T. Brage, I. P. Grant, J. Bieroń, and C. Froese Fischer, Atoms **11**, 7 (2022).

[42] J. Bieroń, C. Froese Fischer, P. Indelicato, P. Jönsson, and P. Pyykkö, Phys. Rev. A **79**, 052502 (2009).

[43] S. Schiffmann and M. Godefroid, J. Quant. Spectrosc. Radiat. Transfer **258**, 107332 (2021).

[44] J. R. Taylor, *An Introduction to Error Analysis: The Study of Uncertainties in Physical Measurements*, 2nd ed. (University Science Books, Sausalito, CA, 1997).

[45] Y. Li, P. Jönsson, M. Godefroid, G. Gaigalas, J. Bieroń, J. P. Marques, P. Indelicato, and C. Chen, Atoms **11**, 4 (2022).

[46] P. Bilous, A. Pálffy, and F. Marquardt, Phys. Rev. Lett. **131**, 133002 (2023).

[47] J. S. Andrews, Multiconfigurational calculations of the transition energy of Lr I (Lu I), Version v1, Zenodo (2025), https://doi.org/10.5281/zenodo.17153930.